

# Fourier Angle Alignment for Oriented Object Detection in Remote Sensing

Changyu Gu<sup>1</sup>      Linwei Chen<sup>2,4,5</sup>      Lin Gu<sup>3</sup>      Ying Fu<sup>1\*</sup>  
<sup>1</sup>Beijing Institute of Technology    <sup>2</sup>University of Hong Kong    <sup>3</sup>Tohoku University  
<sup>4</sup>The Hong Kong University of Science and Technology  
<sup>5</sup>Hong Kong Generative AI Research and Development Center

guchangyu@bit.edu.cn    chenlinwei.ai@gmail.com    lin@tohoku.ac.jp    fuying@bit.edu.cn

## Abstract

In remote sensing rotated object detection, mainstream methods suffer from two bottlenecks, directional incoherence at detector neck and task conflict at detecting head. Utilising fourier rotation equivariance, we introduce **Fourier Angle Alignment**, which analyses angle information through frequency spectrum and aligns the main direction to a certain orientation. Then we propose two plug and play modules : **FAAFusion** and **FAA Head**. **FAAFusion** works at the detector neck, aligning the main direction of higher-level features to the lower-level features and then fusing them. **FAA Head** serves as a new detection head, which pre-aligns RoI features to a canonical angle and adds them to the original features before classification and regression. Experiments on DOTA-v1.0, DOTA-v1.5 and HRSC2016 show that our method can greatly improve previous work. Particularly, our method achieves new state-of-the-art results of 78.72% mAP on DOTA-v1.0 and 72.28% mAP on DOTA-v1.5 datasets with single scale training and testing, validating the efficacy of our approach in remote sensing object detection. The code is made publicly available at <https://github.com/gcy0423/Fourier-Angle-Alignment>.

## 1. Introduction

Compared to general object detection, objects in remote sensing, such as ships, airplanes, and vehicles, are often oriented in arbitrary directions [2, 11, 46]. For rotated object detection (ROD), Oriented Bounding Box (OBB), which simultaneously predicts both the class and the orientation of each object [39, 53], is a popular solution.

Recent progress in ROD focuses on designing rotation-sensitive convolutions [32, 38, 51], modifying the backbone [1, 22, 45] or detection neck [23, 27, 29, 35, 36], or optimizing angle regression losses [14, 37, 43, 44]. In this work, we propose *Fourier Angle Alignment (FAA)* that leverages frequency domain to estimate and align object orientation to

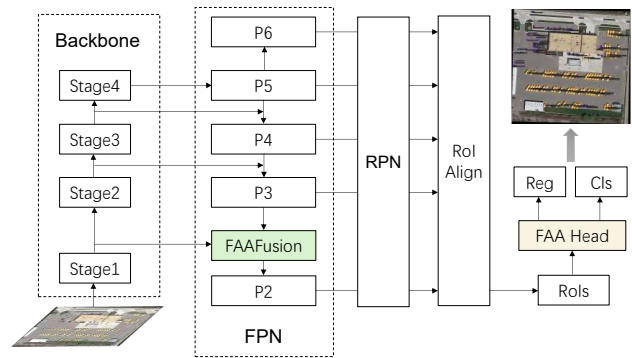


Figure 1. The position of FAAFusion and FAA Head.

enhance existing ROD methods. As shown in Fig.1, our plug-and-play modules can be applied on the main-stream ROD architectures to deal with two common bottlenecks: *directional incoherence in the neck and task conflict in the detection head*.

When giving features from different levels, as shown in Fig.2, traditional FPN [25] fuses them using simple element-wise addition or concatenation. However, on the one hand, features from high levels commonly have strong semantics but blurred spatial details, thus making the orientation coarse and low-frequency [4]. On the other hand, features from low levels have sharp edges and textures, so they carry precise, high-frequency direction cues. When these two types of features are directly fused, their orientation signals often conflict. This mismatch creates noise in the fused features, degrading angle prediction accuracy.

Since the same RoI feature must serve two different tasks, classification and angle regression often conflict. As shown in Fig.3, classification needs rotation-invariant features, for a plane should always be recognized as a plane regardless of its orientation. Regression, however, needs rotation-sensitive features, where the feature must change when the object rotates. Forcing a single feature to satisfy both goals leads to a compromise: the feature becomes

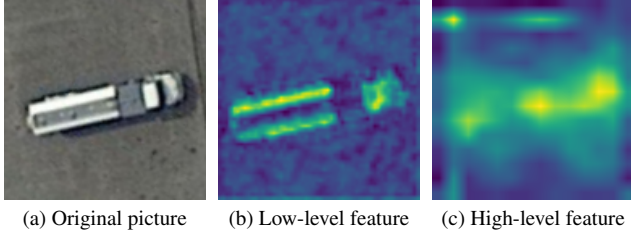


Figure 2. Directional incoherence. High-level feature (c) has strong semantics and large receptive fields but captures the coarse orientation. For example, from (c) we can only infer that the object lies horizontally. Yet many down-samplings blur spatial details, so the orientation signal is low-frequency and vague. Low-level feature (b) keeps rich edges, corners, and textures, giving clear and high-frequency orientation cues.

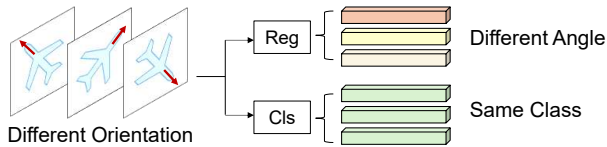


Figure 3. Task conflict in the detection head. As the orientation varies, the angle predictions are expected to be different while the class predictions are expected to be the same.

neither fully invariant nor fully sensitive. This limits the model’s ability to accurately predict both class and angle.

Our FAA comprises two lightweight modules: **FAAFusion** and **FAA Head**. Embedded in the FPN [25], FAA-Fusion first estimates the dominant orientation from low-level features using Fourier analysis and then rotates the high-level features to align them with the low-level features before fusion. This ensures consistent orientation across scales. FAA Head serves as a new detection head. For each RoI features, it estimates the dominant orientation in the frequency domain and rotates the RoI feature to a canonical orientation. Then it adds the rotated feature back to the original one. The aligned feature will benefit the task of classification, while the original feature is helpful for location and orientation regression.

We evaluate our method on three challenging benchmark datasets: DOTA-v1.0 [11], DOTA-v1.5 [11], and HRSC2016 [30]. We select three representative backbones of ResNet50 [18], LSKNet-S [22] and StripNet-S [45] within the Oriented R-CNN [41] framework. Our method improves the mAP of these state-of-the-art methods by 0.68%, 1.00% and 0.63% on DOTA-v1.0 [11], 0.37%, 2.02% and 1.73% on DOTA-v1.5 [11], 2.17%, 1.81% and 1.23% on HRSC2016 [30], proving that frequency-domain orientation estimation is a powerful and practical tool for rotated object detection.

Our main contributions could be summarized as:

- We propose Fourier Angle Alignment, a plug-and-play

framework that leverages frequency-domain analysis to estimate and align object orientations, thereby enhancing existing rotated object detection methods.

- We address directional incoherence at detector neck with the FAAFusion module, which explicitly aligns local features by orientation to ensure directional semantic consistency across scales.
- The FAA Head module replaces detection head and pre-aligns RoI features to a canonical orientation and fuses them with the original features, effectively mitigating the conflict between classification and angle regression.

## 2. Related Works

This section briefly reviews the most relevant studies and methods that have advanced the field, eagerly hoping to lay the foundation for the contributions of this work.

### 2.1. Remote Sensing Object Detection

Given that objects in remote sensing imagery can be oriented in any direction, object detectors must extend beyond the standard outputs of general detection to additionally encode the orientation of the bounding box. Mainstream methods could be summarized as follows. Some studies pay attention to the improvement of the backbone network, replacing the normal convolution block in ResNet [18] with well-designed blocks. ARC [32] introduces an adaptive rotation convolution module which applies multiple groups of rotated kernels to extract features of different orientations. GRA [38] uses group-wise rotating and group-wise attention to relieve the noises produced by the rotated convolution kernels in undesired direction. Some studies focus on building new backbones. As the first method introducing RE-Nets into oriented object detection networks, ReDet [17] proposes ReResNet as a rotation-equivariant backbone to inherently preserve orientation information. LSKNet [22] adaptively captures contextual information of multi-scale and arbitrarily oriented objects in aerial images by introducing a Large Selective Kernel mechanism. PKINet [1] enhances the ability to perceive objects with extreme aspect ratios and varying orientations in aerial images by employing learnable parameterized large convolution kernels. Strip R-CNN [45] employs a strip convolution structure to efficiently model the geometric characteristics of slender objects in aerial images, improving detection performance for high aspect-ratio rotated targets. With the strong feature extraction abilities of their backbone networks, these approaches have vitally enhanced detecting performance.

Other studies concentrate on the neck and detecting head design to better accommodate oriented bounding box (OBB) prediction. While general-purpose necks like PANet [29] and BiFPN [36] enhance cross-scale feature fusion and benefit multi-scale detection, they do not explicitly model orientation. In contrast, top-tier methods inte-

grate orientation awareness into the detection head or RoI processing stage: RoI Transformer [10] learns to transform axis-aligned RoI features into oriented ones via a lightweight spatial transformer, effectively aligning features before regression. Oriented R-CNN [41] adopts a two-stage head that decouples angle prediction from box refinement, achieving high accuracy with low computational overhead. S2A-Net [16] introduces an anchor-free single-stage head with an AlignConv module that dynamically samples features according to predicted angles. Crucially, significant advances have been made in OBB parameterization and regression losses: GWD [43] models OBBs as 2D Gaussian distributions and uses Wasserstein Distance as the loss, while KLD [44] replaces it with Kullback–Leibler Divergence to ensure scale invariance and improve training stability. Despite these impressive results, these approaches primarily operate on spatial-domain features and fail to explicitly encode or learn rotational information directly from the feature representation itself.

## 2.2. Frequency-domain Analysis

Frequency-domain analysis has a long and rich history in computer vision. Early approaches [28, 40, 48] primarily used Fourier properties to design rotation-invariant handcrafted feature extractors, then used these features for downstream tasks. In recent years, with the rise of deep learning, researchers [8, 9, 21, 47, 49] have begun to explicitly integrate Fourier transforms into neural network architectures to exploit their global receptive fields and inherent properties under geometric transformations. For instance, FcaNet [33] replaces global average pooling with a frequency-channel attention mechanism, modeling long-range dependencies in the spectral domain to significantly boost performance in image classification and object detection. More recently, a series of works have underscored the critical role of explicit frequency modeling in dense prediction. Spatial Frequency Modulation [6] mitigates aliasing during downsampling via a modulation-demodulation scheme to preserve high-frequency details. FreqFusion [4] decomposes features into low- and high-frequency components to jointly enhance intra-class consistency and boundary sharpness. Frequency-Adaptive Dilated Convolution [5] dynamically adjusts dilation rates and kernel spectral responses based on local frequency content to balance receptive field size and effective bandwidth. And modules like FDAM [7] counteract the low-pass bias of Vision Transformers through high-frequency attention compensation. Collectively, these advances demonstrate that explicit spectral modeling has established a powerful foundation for improving the performance of feature extraction, thus providing a new view of oriented object detection.

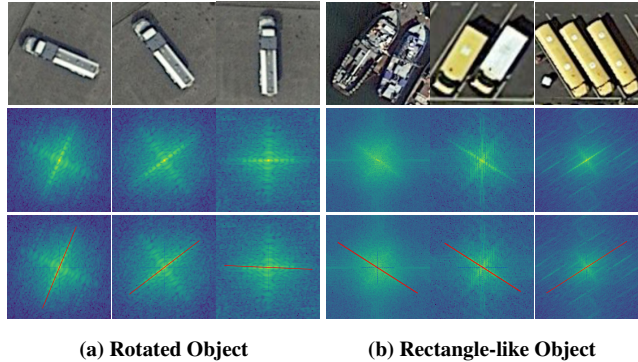


Figure 4. The top row shows the target images in the spatial domain. The second row gives their matching frequency spectra. In the bottom row, red lines point out the main energy directions in each spectrum. (a) If the spatial picture is rotated, its spectrum distribution will be rotated as well. (b) The main spectral direction of one rectangle-like object is perpendicular to the direction of its major axis.

## 3. Methods

In this section, we first introduce our formulation and motivation. Next we describe the detailed method of our Fourier Angle Alignment. Then we will present the applications of FAA at different locations of the detector, FAAFusion and FAA Head, which will be detailed in 3.3 and 3.4.

### 3.1. Formulation and Motivation

**Oriented Object Detection.** Let the input image be  $\mathbf{I}(\mathbf{x})$ ,  $\mathbf{x} = (x, y)^\top$ . For a horizontal object detector  $\mathcal{D}_{\text{HBB}}$ , the output is a set of axis-aligned bounding boxes with class information:

$$\mathcal{D}_{\text{HBB}}(\mathbf{I}) = \{(x_i, y_i, w_i, h_i, c_i)\}, \quad (1)$$

where  $(x_i, y_i)$  is the box center,  $h_i$  and  $w_i$  stand for the height and width of the box, and  $c_i$  is the class of the object in the box.

For an oriented object detector  $\mathcal{D}_{\text{OBB}}$ , the output is a set of rotated bounding boxes that include an orientation angle:

$$\mathcal{D}_{\text{OBB}}(\mathbf{I}) = \{(x_i, y_i, w_i, h_i, \theta_i, c_i)\}, \quad (2)$$

where  $x_i, y_i, w_i, h_i, c_i$  are the same as the HBB, and  $\theta_i$  is the rotation angle.

**Fourier Rotation Equivariance.** Let  $\mathbf{I}(\mathbf{x})$  denote a signal in the spatial domain. Its frequent spectrum is

$$\mathbf{F}(\boldsymbol{\omega}) = \mathcal{F}\{\mathbf{I}(\mathbf{x})\}, \quad (3)$$

where  $\boldsymbol{\omega} = (u, v)^\top$  and  $\mathcal{F}$  means Fourier Transform. Next, consider rotating  $\mathbf{I}$  counterclockwise by an angle  $\phi$  around

the origin, and we can know that the rotated image will be  $\mathbf{I}_\phi(\mathbf{x}) = \mathbf{I}(\mathbf{R}_{-\phi}\mathbf{x})$ , where  $\mathbf{R}_\phi$  is the 2D rotation matrix:

$$\mathbf{R}_\phi = \begin{bmatrix} \cos \phi & -\sin \phi \\ \sin \phi & \cos \phi \end{bmatrix}. \quad (4)$$

Then, suppose the rotated spectrum is  $\mathbf{F}_\phi(\boldsymbol{\omega})$ . By a change of variables, it can finally be inferred that:

$$\mathbf{F}_\phi(\boldsymbol{\omega}) = \mathcal{F}\{\mathbf{I}(\mathbf{R}_{-\phi}\mathbf{x})\} = \mathcal{F}\{\mathbf{I}_\phi(\mathbf{x})\}, \quad (5)$$

which means if a spatial signal is rotated by  $\phi$ , its frequent spectrum will also be rotated by  $\phi$ , as shown in Fig 4a.

**Spectral alignment of rectangles.** Suppose  $\mathbf{I}_{\text{rec}}(\mathbf{x})$  denote a 2D rectangular function in the spatial domain and  $\mathbf{x} = (x, y)^\top$  Specifically,

$$\mathbf{I}_{\text{rec}}(\mathbf{x}) = \begin{cases} 1, & |x| \leq a, |y| \leq b, \\ 0, & \text{otherwise,} \end{cases} \quad (6)$$

with  $0 < b \leq a$ , so that the major axis of the rectangle is aligned with the  $x$ -axis. Its frequent spectrum is

$$\mathbf{F}_{\text{rec}}(\boldsymbol{\omega}) = \mathcal{F}\{\mathbf{I}_{\text{rec}}(\mathbf{x})\}, \quad (7)$$

where  $\boldsymbol{\omega} = (u, v)^\top$  denotes the frequency-domain coordinates. By separability,

$$\mathbf{F}_{\text{rec}}(\boldsymbol{\omega}) = 4ab \cdot \text{sinc}(2au) \cdot \text{sinc}(2bv), \quad (8)$$

where  $\text{sinc}(z) = \sin(\pi z)/(\pi z)$ , and the the power spectrum of the rectangle is

$$|\mathbf{F}_{\text{rec}}(\boldsymbol{\omega})|^2 \propto \text{sinc}^2(2au) \text{sinc}^2(2bv). \quad (9)$$

Since  $a > b$ , the main lobe of  $\text{sinc}(2au)$  is narrower than that of  $\text{sinc}(2bv)$ . Hence, spectral energy decays more slowly along the  $v$ -axis than along the  $u$ -axis. Consequently, in the high-frequency regime, the dominant spectral energy lies along the  $v$ -axis, which is perpendicular to the major axis of the rectangle, as shown in Fig 4b.

**Motivations.** These observations reveal a fundamental property: object orientation can be reliably estimated from the frequency domain. This offers a direct and principled way to handle orientation, which is largely ignored by current detectors that rely only on spatial features.

Specifically, in the neck, low-level features contain sharp edges and textures that encode precise directional cues, while high-level features carry strong semantics but have blurred orientation. Simply adding these features together mixes directionally inconsistent signals, harming angle prediction. Instead, we can use the orientation estimated from low-level features in the frequency domain to explicitly

align the high-level features before fusion, ensuring directional consistency across scales.

Similarly, in the detection head, the same RoI feature is expected to support both classification that benefits from rotation-invariant features and angle regression that needs rotation-sensitive features. This creates an inherent conflict. By estimating the dominant orientation of the RoI in the frequency domain, we can rotate the feature to a canonical pose. The resulting aligned feature becomes nearly rotation-invariant for classification, while the original RoI features is helpful for regression, which could effectively decouple the two conflicted tasks.

### 3.2. Fourier Angle Alignment

We propose Fourier Angle Alignment (FAA), with the main progress shown in Fig.5. Generally speaking, FAA can be divided into two steps: Fourier Angle Estimation and Angle Alignment.

**Fourier Angle Estimation.** With a square feature map  $\mathbf{X} \in \mathbb{R}^{H \times H}$  as input, the FAA estimates its dominant orientation and performs rotational alignment. To begin with, FAA applies a 2D discrete Fourier transform to the input feature map to obtain its spectral representation:

$$\mathbf{F} = \mathcal{F}(\mathbf{X}), \quad (10)$$

where  $\mathcal{F}(\cdot)$  denotes the 2D Fourier transform operator. To facilitate subsequent polar coordinate conversion, FFA shifts the zero-frequency component to the center of the spectrum, which is achieved by multiplying with a phase factor:

$$\mathbf{F}_c(u, v) = \mathbf{F}(u, v) \cdot (-1)^{u+v}, \quad (11)$$

$$u, v = 0, 1, \dots, H - 1.$$

With the intention of estimating the main direction more conveniently, FAA converts the centered spectrum  $\mathbf{F}_c$  from Cartesian coordinates  $(u, v)$  to polar coordinates  $(\rho, \theta)$ , and then computes the corresponding energy spectrum:

$$E(\rho, \theta) = |\mathbf{F}_c(u(\rho, \theta), v(\rho, \theta))|^2, \quad (12)$$

where  $u(\rho, \theta) = \frac{H}{2} + \rho \cos \theta$ ,  $v(\rho, \theta) = \frac{H}{2} + \rho \sin \theta$ ,  $\rho \in [0, \rho_{\text{max}}]$ , and  $\theta \in [0, 2\pi)$ .

Based on our prior knowledge, for a rectangular object, its spectral energy is concentrated around specific orientations. To robustly estimate this dominant orientation, we sum the magnitude spectrum in polar coordinates along the radial direction, thereby obtaining a one-dimensional angular energy distribution function  $E_\theta(\theta)$ :

$$E_\theta(\theta) = \sum_{\rho} \rho \cdot E(\rho, \theta). \quad (13)$$

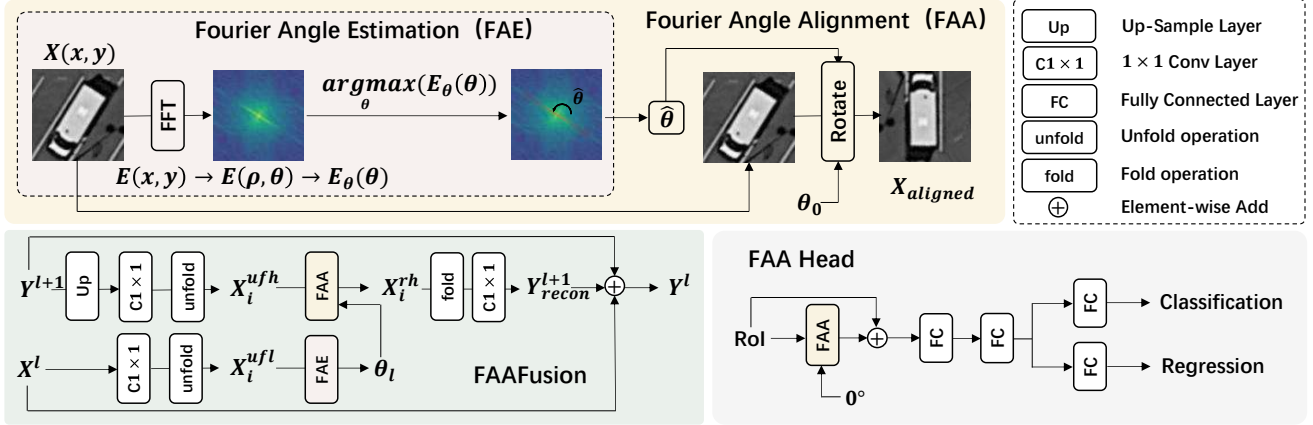


Figure 5. Structures of FAA, FAAFusion and FAA Head. For FAA, it can be divided into two steps. First, we estimate the main direction in frequent domain. And then FAA accepts an external angle and aligns the main direction with it. For FAAFusion, we use the main direction of the lower local feature as the external angle and align the higher local feature with it. For FAA Head, it aligns the main direction of RoI features with  $0^\circ$  to obtain the rotation invariant features.

And the estimated main direction of the object is the direction where the  $E_\theta(\theta)$  reaches maximum. For convenience, we constrain the angular range to  $[0, \pi)$ .

$$\hat{\theta} = \arg \max_{\theta} E_\theta(\theta), \quad (14)$$

**Angle Alignment.** After obtaining the estimated main direction, FAA rotates the original feature map by a specific reference angle to align the main direction with this reference angle:

$$\mathbf{X}_{\text{aligned}} = \mathcal{R}_{\Delta\theta}(\mathbf{X}), \quad (15)$$

where  $\mathcal{R}_{\Delta\theta}(\cdot)$  denotes a 2D rotation operator about the image center.  $\Delta\theta = \theta_0 - \hat{\theta}$ , where  $\theta_0$  is the reference angle.

### 3.3. FAAFusion

FAAFusion replaces the conventional element-wise addition in the FPN [25]. Let the high-level semantic feature be  $\mathbf{Y}^{l+1} \in \mathbb{R}^{C \times H \times W}$  and the low-level detail feature be  $\mathbf{X}^l \in \mathbb{R}^{C \times 2H \times 2W}$ .

First, as in the original FPN [25], we upsample the high-level feature  $\mathbf{Y}^{l+1}$  to match the spatial resolution of the low-level feature  $\mathbf{X}^l$ .

$$\mathbf{Y}_u^{l+1} = \text{Upsample}(\mathbf{Y}^{l+1}). \quad (16)$$

To reduce computational cost, we apply  $1 \times 1$  convolutions to both  $\mathbf{Y}_u^{l+1}$  and  $\mathbf{X}^l$  to project their channel dimensions to a common intermediate size  $C_{mid}$ , and then we use the unfold operation to obtain the local features:

$$\begin{cases} \{\mathbf{p}_i^h\}_{i=1}^N = \text{unfold}(\text{Conv}(\mathbf{Y}_u^{l+1})), \\ \{\mathbf{p}_i^l\}_{i=1}^N = \text{unfold}(\text{Conv}(\mathbf{X}^l)), \end{cases} \quad (17)$$

where  $N = 2H \times 2W$  is the total number of spatial locations, and each local feature  $\mathbf{p}_i^h, \mathbf{p}_i^l$  corresponds to spatial position  $i$ . For  $i$  from 1 to  $N$ , we first estimate the dominant orientation of the lower-level features:

$$\theta_i^l = \text{FAE}(\mathbf{p}_i^l). \quad (18)$$

Then we use  $\theta_i^l$  as the aiming orientation to rotate the higher-level features. The rotated higher-level features are

$$\mathbf{p}_i^{rh} = \text{FAA}(\mathbf{p}_i^h; \theta_i^l). \quad (19)$$

After processing all positions  $i = 1, \dots, N$ , we reconstruct the aligned high-level feature map using the fold operation and apply a  $1 \times 1$  convolution to restore the channel dimension to the output size, resulting in  $\mathbf{Y}_{\text{recon}}^{l+1}$ :

$$\mathbf{Y}_{\text{recon}}^{l+1} = \text{Conv}(\text{fold}(\{\mathbf{p}_i^{rh}\}_{i=1}^N)). \quad (20)$$

Finally, the fused feature at level  $l$  is obtained by summing the low-level feature, the upsampled high-level feature, and the reconstructed aligned feature:

$$\mathbf{Y}^l = \mathbf{X}^l + \mathbf{Y}_u^{l+1} + \mathbf{Y}_{\text{recon}}^{l+1}. \quad (21)$$

### 3.4. FAA Head

The FAA Head serves as a new detection head that directly replaces the original head in the Oriented R-CNN [41] framework. It takes the RoI-aligned feature  $\mathbf{F}_{\text{roi}}$  as input. For each RoI feature, we apply the FAA to align it to a canonical orientation, and specifically,  $0^\circ$  in our experiments:

$$\mathbf{F}_{\text{inv}} = \text{FAA}(\mathbf{F}_{\text{roi}}; 0^\circ). \quad (22)$$

Table 1. Comparisons with state-of-the-art methods on DOTA-v1.0 [11] dataset with single scale training and testing.

Method	Venue	Backbone	PL	BD	BR	GTF	SV	LV	SH	TC	BC	ST	SBF	RA	HA	SP	HC	mAP
R. F-RCNN [34]	TPAMI'16	ResNet50	89.40	81.81	47.28	67.44	73.96	73.12	85.03	90.90	85.15	84.90	56.60	64.77	64.70	70.28	62.22	73.17
R3Det [42]	AAAI'21	ResNet50	89.5	81.2	50.5	66.1	70.9	78.7	78.2	90.8	85.3	84.2	61.8	63.8	68.2	69.8	67.2	73.7
R3Det-GWD [43]	ICML'21	ResNet50	88.82	82.94	55.63	72.75	78.52	83.10	87.46	90.21	86.36	85.44	64.70	61.41	73.46	76.94	57.38	76.34
R3Det-KLD [44]	NIPS'21	ResNet50	88.90	84.17	55.80	69.35	78.72	84.08	87.00	89.75	84.32	85.73	64.74	61.80	76.62	78.49	70.89	77.36
S2ANet [16]	TGRS'21	ResNet50	89.11	82.84	48.37	71.11	78.11	78.39	87.25	90.83	84.90	85.64	60.36	62.60	65.26	69.13	57.94	74.12
RoI Trans. [10]	CVPR'19	ResNet50	89.01	77.48	51.64	72.07	74.43	77.55	87.76	90.81	79.71	85.27	58.36	64.11	76.50	71.99	54.06	74.05
ReDet [17]	CVPR'21	ReResNet	88.79	82.64	53.97	74.00	78.13	84.06	88.04	90.89	87.78	85.75	61.76	60.39	75.96	68.07	63.59	76.25
O-RCNN [41]	IJCV'24	ResNet50	89.46	82.12	54.78	70.86	78.93	83.00	88.20	90.90	87.50	84.68	63.97	67.69	74.94	68.84	52.28	75.87
ARC [32]	ICCV'23	R50-ARC	89.40	82.48	55.33	73.88	79.37	84.05	88.06	90.90	86.44	84.83	63.63	70.32	74.29	71.91	65.43	77.35
GRA [38]	ECCV'24	R50-GRA	—	—	—	—	—	—	—	—	—	—	—	—	—	—	—	77.63
LSKNet [22]	IJCV'24	LSKNet-S	89.66	85.52	57.72	75.70	74.95	78.69	88.24	90.88	86.79	86.38	66.92	63.77	77.77	74.47	64.82	77.49
MutDet [20]	ECCV'24	ResNet50	87.3	78.7	51.3	68.5	78.9	81.6	88.1	90.7	79.9	83.7	58.0	61.8	76.5	72.1	60.8	74.5
PKINet [1]	CVPR'24	PKINet-S	89.72	84.20	55.81	77.63	80.25	84.45	88.12	90.88	87.57	86.07	66.86	70.23	77.47	73.62	62.94	78.39
BGHR [15]	AAAI'25	—	88.21	75.65	42.83	60.17	79.39	74.99	85.76	90.86	83.94	85.34	56.77	65.90	60.18	72.45	49.11	71.44
ReDiffDet [50]	CVPR'25	ResNet50	85.45	77.84	50.39	71.63	80.90	84.85	88.77	90.88	87.00	86.08	63.30	63.43	76.01	76.03	60.16	76.18
ReDiffDet [50]	CVPR'25	Swin-T	82.89	82.90	52.47	70.80	80.48	85.41	88.97	90.90	86.97	87.35	60.24	65.01	76.61	74.28	64.07	76.62
S-RCNN [45]	AAAI'26	StripNet-S	89.56	83.86	53.65	76.27	79.31	84.93	88.24	90.89	87.69	85.88	66.15	68.11	75.73	73.32	67.79	78.09
O-RCNN+ours	-	ResNet50	89.40	84.15	54.66	72.23	78.42	82.89	87.86	90.89	86.26	85.24	63.95	65.58	75.30	70.44	61.06	76.55
LSKNet+ours	-	LSKNet-S	89.85	85.07	55.39	77.77	79.30	84.72	88.56	90.90	87.74	86.29	68.37	67.74	77.19	74.14	64.30	78.49
S-RCNN+ours	-	StripNet-S	89.81	83.27	52.93	77.06	79.57	84.90	88.31	90.89	87.10	86.43	66.43	68.04	75.54	79.03	71.48	<b>78.72</b>

The resulting feature  $\mathbf{F}_{\text{inv}}$  is rotation-invariant and thus more conducive to classification.

To preserve fine-grained spatial cues that may be lost during alignment, we add the original RoI feature back as a residual:

$$\mathbf{F}_{\text{final}} = \mathbf{F}_{\text{inv}} + \mathbf{F}_{\text{roi}}. \quad (23)$$

We then flatten  $\mathbf{F}_{\text{final}}$  into a 1D vector and pass it through two shared fully connected (FC) layers:

$$\mathbf{z} = \text{FC}(\text{FC}(\text{flatten}(\mathbf{F}_{\text{final}}))). \quad (24)$$

Finally, the resulting feature vector  $\mathbf{z}$  is fed into separate classification and regression branches for category prediction and oriented bounding box refinement, respectively.

## 4. Experiments

In this section, we first introduce our experimental settings, including the datasets we used and how we implement our experiments. Then we will exhibit our results on these datasets. In the end of this section is our analysis, consisting of ablation studies, the effectiveness of our FAA Head compared with the latest methods and the analysis of high-IoU performance, which is *de facto* a realistic question.

### 4.1. Experimental Settings

**Datasets.** We conduct our experiments on three popular remote sensing object detection datasets: DOTA-v1.0 [11], DOTA-v1.5 [11] and HRSC2016 [30].

- **DOTA-v1.0** [11] is a large-scale datasets for remote sensing object detection, which includes 2,806 images,

188,282 instances and 15 categories. The dataset is comprised of 1,411, 458, and 937 images for `train`, `val` and `test` sets, respectively.

- **DOTA-v1.5** [11] is an extended version of DOTA-v1.0, which is released for DOAI Challenge 2019. It contains the same 2,806 images but with 403,318 instances and 16 categories, including the refined annotations for vehicle instances and a new category named `Container Crane (CC)`. Moreover, this iteration has a substantial increase of the minuscule instances that are less than 10 pixels, which is more challenging.
- **HRSC2016** [30] is a dataset for ship detection in remote sensing imagery, consisting of 1,061 images and 2,976 ship instances annotated by a horizontal bounding box and an orientation angle. The images are split into 436, 181 and 444 for `train`, `val` and `test` sets.

**Evaluation Metrics.** Followed by previous works [1, 22, 41, 45], we employ the mean Average Precision (mAP) as our evaluation metrics for the two DOTA [11] datasets. As for HRSC2016 [30], we evaluate our results with PASCAL VOC2007 [12]/VOC2012 [13] metrics with AP50, AP75 and mAP reported, according to the preceding work [38].

**Implementation details.** All the experiments are implemented under the MMRotate [52] toolbox developed by Openmmlab. Followed by previous works [1, 22, 41, 45], for DOTA-v1.0 [11] and DOTA-v1.5 [11], the input size is set to  $1024 \times 1024$ , and for HRSC2016, the input size is set to  $800 \times 800$ . For DOTA-v1.0 [11] and DOTA-v1.5 [11], training is conducted for 16 epochs on `trainval` set. Models from epochs 12 to 16 are evaluated on `test` set, and the best-performing one is selected as the final result. For HRSC2016 [30], training is conducted for 36 epochs

Table 2. Comparisons with state-of-the-art methods on DOTA-v1.5 [11] dataset with single scale training and testing.

Method	Backbone	PL	BD	BR	GTF	SV	LV	SH	TC	BC	ST	SBF	RA	HA	SP	HC	CC	mAP
RetinaNet-O [26]	ResNet50	71.43	77.64	42.12	64.65	44.53	56.79	73.31	90.84	76.02	59.96	46.95	69.24	59.65	64.52	48.06	0.83	59.16
R. F-RCNN [34]	ResNet50	71.89	74.47	44.45	59.87	51.28	68.98	79.37	90.78	77.38	67.50	47.75	69.72	61.22	65.28	60.47	1.54	62.00
Mask R-CNN [19]	ResNet50	76.84	73.51	49.90	57.80	51.31	71.34	79.75	90.46	74.21	66.07	46.21	70.61	63.07	64.46	57.81	9.42	62.67
HTC [3]	-	77.80	73.67	51.40	63.99	51.54	73.31	80.31	90.48	75.12	67.34	48.51	70.63	64.84	64.48	55.87	5.15	63.40
RoI Trans. [10]	ResNet50	71.70	82.70	53.00	71.50	51.30	74.60	80.60	90.40	78.00	68.30	53.10	73.40	73.90	65.60	56.90	3.00	65.50
O-RCNN [41]	ResNet50	79.68	81.72	53.36	72.17	52.26	76.47	81.00	90.86	78.93	68.18	65.05	72.17	67.68	65.23	56.11	7.42	66.77
ReDet [17]	ReResNet	79.20	82.81	51.92	71.41	52.38	75.73	80.92	90.83	75.81	68.64	49.29	72.03	73.36	70.55	63.33	11.53	66.86
S-RCNN [45]	StripNet-S	80.31	82.24	53.91	76.61	52.39	81.55	87.82	90.89	82.44	66.32	61.58	73.27	75.04	65.84	73.42	13.85	69.84
LSKNet [22]	LSKNet-S	72.05	84.94	55.41	74.93	52.42	77.45	81.17	90.85	79.44	69.00	62.10	73.72	77.49	75.29	55.81	42.19	70.26
PKINet [1]	PKINet-S	80.31	85.00	55.61	74.38	52.41	76.85	88.38	90.87	79.04	68.78	67.47	72.45	76.24	74.53	64.07	37.13	71.47
O-RCNN+ours	ResNet50	79.62	81.14	53.96	73.78	52.20	76.80	81.17	90.90	78.47	68.55	64.21	73.72	68.26	64.64	54.09	12.85	67.14
S-RCNN+ours	StripNet-S	80.14	82.02	51.89	76.42	52.52	81.45	88.21	90.88	85.76	68.52	62.34	72.68	74.01	74.97	71.20	32.10	71.57
LSKNet+ours	LSKNet-S	80.69	85.34	55.42	77.91	52.64	82.26	88.48	90.85	86.38	69.32	62.04	74.11	75.83	74.70	73.18	27.30	<b>72.28</b>

and the last weight is used for testing. During the training progress, we use AdamW [31] as the optimizer with the weight decay set to 0.05. The initial learning rate is set to 0.0004 for HRSC2016 [30] and 0.0001 for the two DOTA [11] datasets. With a batch size of 2, all training and testing are performed on a single RTX 3090 GPU.

## 4.2. Main Results

We first add our FAAFusion and FAA Head to three representative state-of-the-art methods within the Oriented R-CNN [41] framework on the datasets mentioned above. Among these methods, ResNet50 [18] is the most classic and popular backbone, which is widely used or modified not only in object detection tasks but also in other computer vision tasks. LSKNet-S [22] is recently the most powerful in both detection and segmentation, and StripNet-S [45] is the latest state-of-the-art method.

**Results on DOTA-v1.0 [11].** As shown in Table 1, we choose ResNet50 [18], LSKNet-S [22] and StripNet-S [45] as the backbone, and add our FAAFusion and FAA Head into the model. Specially, for Strip R-CNN [45] who has designed the Strip Head, we replace their Strip Head with our FAA Head. Based on these models, our methods achieve new improvements of +0.68%, +1.00% and +0.63%, respectively. Compared to current state-of-the-art method PKINet [1], our results using StripNet-S [45] achieve new sota result of 78.72%, with 0.33% higher on mAP.

**Results on DOTA-v1.5 [11].** Similarly, we choose ResNet50 [18], LSKNet-S [22] and StripNet-S [45] as the backbone, and add our FAAFusion and FAA Head into the model. For Strip R-CNN [45], we replace their Strip Head with our FAA Head as before. As shown in Table 2, based on these models, our methods achieve new improvements of 67.14%, 71.57% and 72.28%, with the increase of 0.37%, 1.73% and 2.02% on each models, respectively. Compared to current two-stage sota detector PKINet [1], our results using LSKNet-S [45] achieve new sota result of 72.28%,

with 0.81% higher on mAP.

**Results on HRSC2016 [30].** As shown in Table 3, we integrate our FAAFusion and FAA Head into three representative oriented object detectors: Oriented R-CNN [41], LSKNet [22] and Strip R-CNN [45]. Followed by these works, we report the AP50 within the evaluation protocols of PASCAL VOC2007 [12] and VOC2012 [13]. Moreover, to compare the detection performance of the model under stricter criteria, we also report the AP75 as well as mAP results of COCO [24] style. Under the VOC2007 [12] metric, our method consistently improves performance across all baselines, achieving mAP gains of 2.17%, 1.81% and 1.23%, respectively. Under the VOC2012 [13] metric, our approach boosts mAP by 1.72% for Oriented R-CNN [41], 2.34% for LSKNet [22], and maintains competitive performance of 0.43% higher for Strip R-CNN [45].

## 4.3. Analysis

**Ablation study of the two proposed modules.** To measure the effectiveness of FAAFusion and FAA Head, we conduct ablation experiments on Oriented R-CNN [41] framework with LSKNet-S [22] as the backbone. We replace the element-wise add with our FAAFusion when fusing the third-level and second-level features in FPN [25] and change the original detection head to FAA Head. The FAA Head follows the detection head design of Oriented R-CNN [41] framework, using two shared fully connected layers before classification and regression. But different from the original output dimension of the first fully connected layer that is set to 1024, the output dimension of our FAA Head is set to 1024 + 256. As shown in Table 4, we evaluate the impact of the FAAFusion and FAA Head on DOTA-v1.0 [11] dataset. Results show that FAAFusion and FAA Head respectively improve the performance of LSKNet [22] by 0.42% and 0.78%, which means both of our two modules could make contributions to the results.

**Comparison with the latest work of detection head.**

Table 3. Comparisons with three representative state-of-the-art methods on HRSC2016 [30] dataset. The values of APs are calculated with PASCAL VOC2007 [12]/VOC2012 [13] metrics and the mAPs are reported with COCO [24] styles. All the models are retrained and tested on a single RTX 3090. The Params and FLOPs are calculated with MMRotate [52] toolbox.

Method	#Params↓	#FLOPs↓	AP50↑	AP75↑	mAP↑
PASCAL VOC2007 [12]					
O-RCNN [41]	41.13M	134.46G	89.7	79.5	64.77
O-RCNN+ours	63.27M	140.70G	89.8	80.0	<b>66.94</b>
LSKNet [22]	30.96M	111.42G	90.2	87.9	68.78
LSKNet+ours	48.34M	114.89G	90.6	89.8	<b>70.74</b>
S-RCNN [45]	45.12M	157.19G	89.5	78.8	69.18
S-RCNN+ours	49.05M	115.91G	90.0	78.6	<b>70.41</b>
PASCAL VOC2012 [13]					
O-RCNN [41]	41.13M	134.46G	96.3	84.1	67.80
O-RCNN+ours	63.27M	140.70G	95.9	85.9	<b>69.52</b>
LSKNet [22]	30.96M	111.42G	97.8	89.2	72.37
LSKNet+ours	48.34M	114.89G	98.3	91.8	<b>74.71</b>
S-RCNN [45]	45.12M	157.19G	97.7	87.6	72.56
S-RCNN+ours	49.05M	115.91G	98.2	89.7	<b>72.99</b>

Table 4. Ablation study. We conducted the experiment with LSKNet-S [22] as the backbone. The Params and FLOPs are calculated with MMRotate [52] toolbox.

FAAFusion	FAA Head	#Params↓	#FLOPs↓	mAP↑
✗	✗	30.98M	173.68G	77.49
✗	✓	48.35M	177.15G	78.27
✓	✗	32.18M	175.59G	77.91
✓	✓	49.56M	179.06G	<b>78.49</b>

To evaluate the effectiveness of our FAA Head, we verify the detection head on three representative backbones: ResNet50 [18], LSKNet-S [22] and StripNet-S [45]. Specifically, we choose the latest detection head, the Strip Head [45], together with the original detection head, as our comparison. As shown in Table 5, across all these three detectors, the FAA Head achieves the highest mAP value. Compared with the Strip Head [45], FAA Head achieves higher mAP with very close parameters but much lower computational cost. These results indicate that the FAA Head can consistently improve detection performance without substantially increasing the computational cost.

**Analysis of high-IoU performance.** In the current evaluation protocol for rotated ship detection, the results of AP50 are almost saturated. Differences among methods are tiny and hide true fine-localization ability. Once the IoU threshold rises above 0.7, the performance of mainstream detectors drops sharply, showing that their geometric modeling is still coarse. Tasks such as ship detection, however, highly

Table 5. Comparison with other detecting head on other remote sensing object detectors. The Params and FLOPs are calculated with MMRotate [52] toolbox.

Method	Detecting Head	#Params↓	#FLOPs↓	mAP↑
O-RCNN [41]	Original Head	41.14M	211.43G	75.81
	Strip Head	55.82M	258.35G	76.11
	FAA Head	58.51M	214.90G	<b>76.18</b>
LSKNet [22]	Original Head	30.98M	173.68G	77.49
	Strip Head	45.65M	220.60G	78.04
	FAA Head	48.35M	177.15G	<b>78.27</b>
S-RCNN [45]	Original Head	30.46M	171.79G	77.03
	Strip Head	45.14M	218.71G	78.09
	FAA Head	47.83M	175.26G	<b>78.52</b>

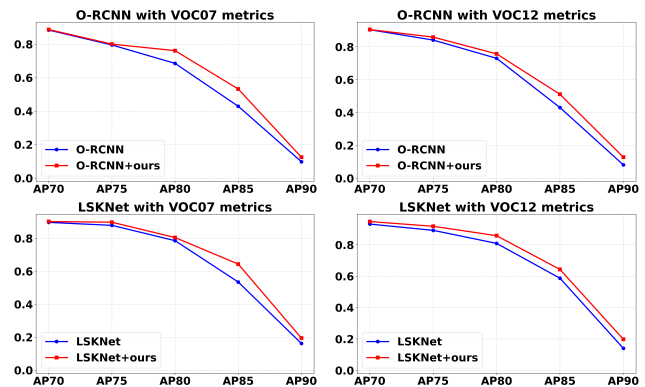


Figure 6. Effectiveness of our method at Oriented R-CNN [41] and LSKNet [22] compared to the original methods on HRSC2016 [30] dataset. In the high IoU threshold range, our method performs better. The AP values are calculated with PASCAL VOC2007 [12] and VOC 2012 [13] metrics.

demand strict box fitting and accurate orientation, because small misalignments could lead to later recognition or ranging errors. Testing robustness in the high-IoU range therefore removes the artificial advantage given by loose metrics and directly checks whether a model is well-performed in precision-critical scenes. Driven by this consideration, we compute AP of high IoU thresholds from 0.70 to 0.90 and plot the curves. As illustrated in Figure 6, the advantage of our method becomes increasingly evident at higher IoU thresholds, demonstrating its superior capability in precise orientation modeling.

## 5. Conclusion

In this work, we propose Fourier Angle Alignment, leveraging fourier rotation equivariance and spectral alignment of rectangles to better model orientation cues in oriented object detection tasks. We theoretically show that the spectral energy of a rectangular object concentrates perpendicular to its major axis, and use this insight to estimate dominant

orientations in the frequency domain and align features accordingly. We integrate FAA into both neck and the detecting head, designing FAAFusion and FAA Head, which enhance orientation consistency across scales and improve rotation invariance of RoI features with minimal computational overhead. Experiments on three benchmark datasets demonstrate the efficacy of our approach in remote sensing object detection. In the future, it is worth exploring the generalization of FAA to other vision tasks such as instance segmentation or remote sensing changing detection, and investigate more efficient frequency-domain alignment strategies for real-time applications.

## References

- [1] Xinhao Cai, Qiuxia Lai, Yuwei Wang, Wenguan Wang, Zeren Sun, and Yazhou Yao. Poly kernel inception network for remote sensing detection. In *IEEE Computer Vision and Pattern Recognition Conference*, pages 27706–27716, 2024. 1, 2, 6, 7
- [2] Guang Chen, Haitao Wang, Kai Chen, Zhijun Li, Zida Song, Yinlong Liu, Wenkai Chen, and Alois Knoll. A survey of the four pillars for small object detection: Multiscale representation, contextual information, super-resolution, and region proposal. *IEEE Transactions on Systems, Man, and Cybernetics: Systems*, 52(2):936–953, 2022. 1
- [3] Kai Chen, Jiangmiao Pang, Jiaqi Wang, Yu Xiong, Xiaoxiao Li, Shuyang Sun, Wansen Feng, Ziwei Liu, Jianping Shi, Wanli Ouyang, Chen Change Loy, and Dahua Lin. Hybrid task cascade for instance segmentation. In *IEEE Computer Vision and Pattern Recognition Conference*, pages 4969–4978, 2019. 7
- [4] Linwei Chen, Ying Fu, Lin Gu, Chenggang Yan, Tatsuya Harada, and Gao Huang. Frequency-aware feature fusion for dense image prediction. *IEEE Transactions on Pattern Analysis and Machine Intelligence*, 46(12):10763–10780, 2024. 1, 3
- [5] Linwei Chen, Lin Gu, Dezhi Zheng, and Ying Fu. Frequency-adaptive dilated convolution for semantic segmentation. In *IEEE Computer Vision and Pattern Recognition Conference*, pages 3414–3425, 2024. 3
- [6] Linwei Chen, Ying Fu, Lin Gu, Dezhi Zheng, and Jifeng Dai. Spatial frequency modulation for semantic segmentation. *IEEE Transactions on Pattern Analysis and Machine Intelligence*, 47(11):9767–9784, 2025. 3
- [7] Linwei Chen, Lin Gu, and Ying Fu. Frequency-dynamic attention modulation for dense prediction. In *IEEE International Conference on Computer Vision*, pages 22620–22632, 2025. 3
- [8] Linwei Chen, Lin Gu, Liang Li, Chenggang Yan, and Ying Fu. Frequency dynamic convolution for dense image prediction. In *IEEE Computer Vision and Pattern Recognition Conference*, pages 1–11, 2025. 3
- [9] Yuning Cui, Wenqi Ren, Xiaochun Cao, and Alois Knoll. Image restoration via frequency selection. *IEEE Transactions on Pattern Analysis and Machine Intelligence*, 46(2):1093–1108, 2024. 3
- [10] Jian Ding, Nan Xue, Yang Long, Gui-Song Xia, and Qikai Lu. Learning roi transformer for oriented object detection in aerial images. In *IEEE Computer Vision and Pattern Recognition Conference*, pages 2849–2858, 2019. 3, 6, 7
- [11] Jian Ding, Nan Xue, Gui-Song Xia, Xiang Bai, Wen Yang, Michael Yang, Serge Belongie, Jiebo Luo, Mihai Datcu, Marcello Pelillo, and Liangpei Zhang. Object detection in aerial images: A large-scale benchmark and challenges. *IEEE Transactions on Pattern Analysis and Machine Intelligence*, pages 1–1, 2021. 1, 2, 6, 7
- [12] M. Everingham, L. Van Gool, C. K. I. Williams, J. Winn, and A. Zisserman. The PASCAL Visual Object Classes Challenge Results. <http://www.pascal-network.org/challenges/VOC/voc2007/workshop/index.html>, 2007. 6, 7, 8
- [13] M. Everingham, L. Van Gool, C. K. I. Williams, J. Winn, and A. Zisserman. The PASCAL Visual Object Classes Challenge Results. <http://www.pascal-network.org/challenges/VOC/voc2012/workshop/index.html>, 2012. 6, 7, 8
- [14] Xiaoxu Feng, Xiwen Yao, Gong Cheng, Jungong Han, and Junwei Han. Saenet: Self-supervised adversarial and equivariant network for weakly supervised object detection in remote sensing images. *IEEE Transactions on Geoscience and Remote Sensing*, 60:1–11, 2022. 1
- [15] Chenlin Fu and Yingying Zhu. Bghr: bridging the gap between hbox-supervised and rbox-supervised oriented object detection via adaptive fine-grained sample mining. In *AAAI Conference on Artificial Intelligence*. AAAI Press, 2025. 6
- [16] J. Han, J. Ding, J. Li, and G. S. Xia. Align deep features for oriented object detection. *IEEE Transactions on Geoscience and Remote Sensing*, pages 1–11, 2021. 3, 6
- [17] Jiaming Han, Jian Ding, Nan Xue, and Gui-Song Xia. Redet: A rotation-equivariant detector for aerial object detection. In *IEEE Computer Vision and Pattern Recognition Conference*, pages 2786–2795, 2021. 2, 6, 7
- [18] Kaiming He, Xiangyu Zhang, Shaoqing Ren, and Jian Sun. Deep residual learning for image recognition. In *IEEE Computer Vision and Pattern Recognition Conference*, pages 770–778, 2016. 2, 7, 8
- [19] Kaiming He, Georgia Gkioxari, Piotr Dollár, and Ross Girshick. Mask r-cnn. In *IEEE International Conference on Computer Vision*, pages 2980–2988, 2017. 7
- [20] Ziyue Huang, Yongchao Feng, Qingjie Liu, and Yunhong Wang. Mutdet: Mutually optimizing pre-training for remote sensing object detection. In *European Conference on Computer Vision*, 2024. 6
- [21] Hesong Li, Ziqi Wu, Ruiwen Shao, Tao Zhang, and Ying Fu. Noise calibration and spatial-frequency interactive network for stem image enhancement. In *IEEE Computer Vision and Pattern Recognition Conference*, pages 21287–21296, 2025. 3
- [22] Yuxuan Li, Xiang Li, Yimain Dai, Qibin Hou, Li Liu, Yongxiang Liu, Ming-Ming Cheng, and Jian Yang. Lsknet: A foundation lightweight backbone for remote sensing. *International Journal of Computer Vision*, 2024. 1, 2, 6, 7, 8

- [23] Qifeng Lin, Jianhui Zhao, Bo Du, Gang Fu, and Zhiyong Yuan. Mednet: Multiexpert detection network with unsupervised clustering of training samples. *IEEE Transactions on Geoscience and Remote Sensing*, 60:1–14, 2022. 1
- [24] Tsung-Yi Lin, Michael Maire, Serge Belongie, Lubomir Bourdev, Ross Girshick, James Hays, Pietro Perona, Deva Ramanan, C Lawrence Zitnick, and Piotr Dollár. Microsoft coco: Common objects in context. In *European Conference on Computer Vision*, pages 740–755. Springer, 2014. 7, 8
- [25] Tsung-Yi Lin, Piotr Dollár, Ross Girshick, Kaiming He, Bharath Hariharan, and Serge Belongie. Feature pyramid networks for object detection. In *IEEE Computer Vision and Pattern Recognition Conference*, pages 936–944, 2017. 1, 2, 5, 7
- [26] Tsung-Yi Lin, Priya Goyal, Ross Girshick, Kaiming He, and Piotr Dollár. Focal loss for dense object detection. In *IEEE International Conference on Computer Vision*, pages 2999–3007, 2017. 7
- [27] Junmin Liu, Shijie Li, Changsheng Zhou, Xiangyong Cao, Yong Gao, and Bo Wang. Sraf-net: A scene-relevant anchor-free object detection network in remote sensing images. *IEEE Transactions on Geoscience and Remote Sensing*, 60: 1–14, 2022. 1
- [28] Kun Liu, Henrik Skibbe, Thorsten Schmidt, Thomas Blein, Klaus Palme, Thomas Brox, and Olaf Ronneberger. Rotation-invariant hog descriptors using fourier analysis in polar and spherical coordinates. *International Journal of Computer Vision*, 46(106):342–364, 2014. 3
- [29] Shu Liu, Lu Qi, Haifang Qin, Jianping Shi, and Jiaya Jia. Path aggregation network for instance segmentation. In *IEEE Computer Vision and Pattern Recognition Conference*, 2018. 1, 2
- [30] Zikun Liu., Liu Yuan., Lubin Weng., and Yiping Yang. A high resolution optical satellite image dataset for ship recognition and some new baselines. In *International Conference on Pattern Recognition Applications and Methods*, pages 324–331. INSTICC, SciTePress, 2017. 2, 6, 7, 8
- [31] Ilya Loshchilov and Frank Hutter. Decoupled weight decay regularization. In *International Conference on Learning Representations*, 2017. 7
- [32] Yifan Pu, Yiru Wang, Zhuofan Xia, Yizeng Han, Yulin Wang, Weihao Gan, Zidong Wang, Shiji Song, and Gao Huang. Adaptive rotated convolution for rotated object detection. In *IEEE International Conference on Computer Vision*, 2023. 1, 2, 6
- [33] Zequn Qin, Pengyi Zhang, Fei Wu, and Xi Li. Fcanet: Frequency channel attention networks. In *IEEE International Conference on Computer Vision*, pages 763–772, 2021. 3
- [34] Shaoqing Ren, Kaiming He, Ross Girshick, and Jian Sun. Faster r-cnn: Towards real-time object detection with region proposal networks. *IEEE Transactions on Pattern Analysis and Machine Intelligence*, 39(6):1137–1149, 2017. 6, 7
- [35] Pourya Shamsolmoali, Jocelyn Chanussot, Masoumeh Zareapoor, Huiyu Zhou, and Jie Yang. Multipatch feature pyramid network for weakly supervised object detection in optical remote sensing images. *IEEE Transactions on Geoscience and Remote Sensing*, 60:1–13, 2022. 1
- [36] Mingxing Tan, Ruoming Pang, and Quoc V. Le. Efficientdet: Scalable and efficient object detection. In *IEEE Computer Vision and Pattern Recognition Conference*, pages 10778–10787, 2020. 1, 2
- [37] Hao Wang, Zhanchao Huang, Zhengchao Chen, Ying Song, and Wei Li. Multigrained angle representation for remote-sensing object detection. *IEEE Transactions on Geoscience and Remote Sensing*, 60:1–13, 2022. 1
- [38] Jiangshan Wang, Yifan Pu, Yizeng Han, Jiayi Guo, Yiru Wang, Xiu Li, and Gao Huang. Gra: Detecting oriented objects through group-wise rotating and attention. In *European Conference on Computer Vision*, 2024. 1, 2, 6
- [39] Kun Wang, Zi Wang, Zhang Li, Ang Su, Xichao Teng, Erting Pan, Minhao Liu, and Qifeng Yu. Oriented object detection in optical remote sensing images using deep learning: a survey. *Artificial Intelligence Review*, 58(11), 2025. 1
- [40] Xin Wu, Danfeng Hong, Jocelyn Chanussot, Yang Xu, Ran Tao, and Yue Wang. Fourier-based rotation-invariant feature boosting: An efficient framework for geospatial object detection. *IEEE Geoscience and Remote Sensing Letters*, 17(2):302–306, 2020. 3
- [41] Xingxing Xie, Gong Cheng, Jiabao Wang, Xiwen Yao, and Junwei Han. Oriented r-cnn for object detection. In *IEEE International Conference on Computer Vision*, pages 3520–3529, 2021. 2, 3, 5, 6, 7, 8
- [42] Xue Yang, Junchi Yan, Ziming Feng, and Tao He. R3det: Refined single-stage detector with feature refinement for rotating object. In *AAAI Conference on Artificial Intelligence*, pages 3163–3171, 2021. 6
- [43] Xue Yang, Junchi Yan, Ming Qi, Wentao Wang, Zhang Xiaopeng, and Tian Qi. Rethinking rotated object detection with gaussian wasserstein distance loss. In *International Conference on Machine Learning*, 2021. 1, 3, 6
- [44] Xue Yang, Xiaojiang Yang, Jirui Yang, Qi Ming, Wentao Wang, Qi Tian, and Junchi Yan. Learning high-precision bounding box for rotated object detection via kullback-leibler divergence. In *Conference on Neural Information Processing Systems*, 2021. 1, 3, 6
- [45] Xinbin Yuan, ZhaoHui Zheng, Yuxuan Li, Xialei Liu, Li Liu, Xiang Li, Qibin Hou, and Ming-Ming Cheng. Strip r-cnn: Large strip convolution for remote sensing object detection. *arXiv preprint arXiv:2501.03775*, 2025. 1, 2, 6, 7, 8
- [46] Xiangrong Zhang, Tianyang Zhang, Guanchun Wang, Peng Zhu, Xu Tang, Xiuping Jia, and Licheng Jiao. Remote sensing object detection meets deep learning: A metareview of challenges and advances. *IEEE Geoscience and Remote Sensing Magazine*, 11(4):8–44, 2023. 1
- [47] Yingkai Zhang, Zeqiang Lai, Tao Zhang, Ying Fu, and Chenghu Zhou. Unaligned rgb guided hyperspectral image super-resolution with spatial-spectral concordance. *International Journal of Computer Vision*, 133(9):6590–6610, 2025. 3
- [48] Yingkai Zhang, Tao Zhang, Jing Nie, and Ying Fu. Real noise decoupling for hyperspectral image denoising. *arXiv preprint arXiv:2511.17196*, 2025. 3
- [49] Yingkai Zhang, Shuang Chen, Ye Tian, Yunyi Gao, Jianyong Jiang, and Ying Fu. Supervise-assisted multi-modality

fusion diffusion model for pet restoration. *arXiv preprint arXiv:2602.11545*, 2026. [3](#)

- [50] Jiaqi Zhao, Zeyu Ding, Yong Zhou, Hancheng Zhu, Wen-Liang Du, and Rui Yao. Rediffdet: Rotation-equivariant diffusion model for oriented object detection. In *IEEE Computer Vision and Pattern Recognition Conference*, pages 24429–24439, 2025. [6](#)
- [51] Xudong Zhao, Ran Tao, Wei Li, Wilfried Philips, and Wenzhi Liao. Fractional gabor convolutional network for multi-source remote sensing data classification. *IEEE Transactions on Geoscience and Remote Sensing*, 60:1–18, 2022. [1](#)
- [52] Yue Zhou, Xue Yang, Gefan Zhang, Jiabao Wang, Yanyi Liu, Liping Hou, Xue Jiang, Xingzhao Liu, Junchi Yan, Chengqi Lyu, Wenwei Zhang, and Kai Chen. Mmrotate: A rotated object detection benchmark using pytorch. In *ACM International Conference on Multimedia*, 2022. [6](#), [8](#)
- [53] Zhengxia Zou, Keyan Chen, Zhenwei Shi, Yuhong Guo, and Jieping Ye. Object detection in 20 years: A survey. *Proceedings of the IEEE*, 111(3):257–276, 2023. [1](#)